



# The role of exposed facets in the Fenton-like reactivity of CeO<sub>2</sub> nanocrystal to the Orange II

Chengjie Zang, Xiansong Zhang, Shiyu Hu, Feng Chen \*

Key Laboratory for Advanced Materials and Institute of Fine Chemicals, School of Chemistry and Molecular Engineering, East China University of Science and Technology, 130 Meilong Road, Shanghai, 200237, China

## ARTICLE INFO

### Article history:

Received 28 February 2017

Received in revised form 4 May 2017

Accepted 23 May 2017

Available online 25 May 2017

### Keywords:

Fenton-like reaction

Kinetics

Crystal facet

CeO<sub>2</sub> nanorod

CeO<sub>2</sub> nanocube

## ABSTRACT

Recently, ceria-based Fenton-like reactions have been developing in wastewater treatment. Nevertheless, the effects of geometric (exposed facets) of the CeO<sub>2</sub> on its Fenton-like reactivity have rarely been considered. In this work, shaped CeO<sub>2</sub> nanocrystals with different exposed facets were synthesized and applied in the Fenton-like degradation of Orange II (AO7). Due to the relative low oxygen vacancy formation energy on {110} facet, H<sub>2</sub>O<sub>2</sub> decomposition shows higher apparent activation energy with nanocubes ({100} facet) than that with nanorods ({110} and {100} facets). CeO<sub>2</sub> nanorods calcined at 300 °C exhibits the maximal activity for the decomposition of H<sub>2</sub>O<sub>2</sub>, while that for the Fenton-like degradation of AO7 is achieved with CeO<sub>2</sub> nanorods calcined at 500 °C. Calcination at higher temperature decreases the surface Ce(III) content of CeO<sub>2</sub>, thus lowers the H<sub>2</sub>O<sub>2</sub> decomposition rate. On the contrary, the decrescent formation energy of oxygen vacancy, the decreased amount of surface hydroxyls, as well as reduced coordination status of surface Ce cations, play important roles in promoting the adsorption and Fenton-like degradation of AO7 for CeO<sub>2</sub> nanorods calcined at 500 °C.

© 2017 Elsevier B.V. All rights reserved.

## 1. Introduction

Advanced oxidation processes (AOPs) such as Fenton and Fenton-like processes are emerging alternative technologies for efficiently removing water-soluble VOCs of high chemical stability and low-biodegradability [1]. Limited by the narrow working pH range (<4), separation and recovery of the iron species, homogeneous Fenton reaction [2] always became disable in dealing with various complex situations. Therefore, non-ferrous heterogeneous Fenton-like reaction has recently been attracting widespread attention as its high chemical stability and wider working pH range such as MnO<sub>2</sub>-based and CeO<sub>2</sub>-based Fenton-like process [3,4].

As an important rare earth material, cerium oxides (CeO<sub>2</sub>) has been widely applied in many fields including soot combustion catalysts [5], water gas shift (WGS) reactions [6], automotive three-way catalysts [7], solid oxide fuel cells [8] and steam reforming [9]. The abundant oxygen vacancies and low redox potential promote a perfect performance in its catalytic oxidation applications [10]. Particularly, the application of CeO<sub>2</sub> has recently been extended to the wastewater treatment as a heterogeneous Fenton-like catalyst [4,11–14]. Wang [12] suggested that the presence of Ce(III)

could induce charge imbalance, oxygen vacancies, and unsaturated chemical bonds on the surface of CeO<sub>2</sub>, which play a certain role in heterogeneous Fenton-like reaction. Hao [13] demonstrated that the adsorbed amount of H<sub>2</sub>O<sub>2</sub> on CeO<sub>2</sub> increases greatly due to the formation of oxygen vacancies, which is of significance to produce active oxygen species and then to degrade pollutants. According to our previous studies [4,11,15], interfacial peroxide species formed by the complexation of H<sub>2</sub>O<sub>2</sub> with Ce(III) sites on the surface of CeO<sub>2</sub> could induce an intermolecular rearrangement with the neighboring adsorbed organic substance to achieve the oxidation of organics. The catalytic degradation efficiency of CeO<sub>2</sub> greatly depends on its adsorption capacity to the organic molecules and the generation rate of active oxygen species [11,15]. However, these researches mainly focus on the enhanced Fenton-like reactivity by adjusting the surface chemical composition and oxygen vacancy concentrations, while the survey of some other important surface factors such as exposed crystal facet and hydroxyl coverage is barely reported, although they are also deemed to affect the catalytic performance in interfacial reaction process [16,17].

In the recent decade, CeO<sub>2</sub> with special crystal shapes, such as nanorods (exposing {110} and {100} facets) and nanocubes (exposing {100} facet) has been attracting great interest in many applications for its enhanced catalytic performances [18–21]. Extensive experimental studies [18,22,23] have been devoted to understanding CO oxidation over CeO<sub>2</sub> catalysts. The results

\* Corresponding author.

E-mail address: [fengchen@ecust.edu.cn](mailto:fengchen@ecust.edu.cn) (F. Chen).

showed that CO interaction with ceria is structure dependent and  $\text{CeO}_2$  nanocrystals exposing reactive  $\{110\}$  and  $\{100\}$  planes on the surface are more active for CO oxidation than those dominated by  $\{111\}$  surfaces. Theoretical studies demonstrate that the formation energy of oxygen vacancy, as well as the nature and the content of defect sites, greatly affects the catalytic activity of  $\text{CeO}_2$  for different lattice planes. Generally, the formation energy of oxygen vacancy for different exposing  $\text{CeO}_2$  planes follows the order of  $\{110\} < \{100\} < \{111\}$  [24,25], while Chen et al. [26] predicted theoretically that the surface energy of exposing  $\{100\}$  crystal plane can be lowered in the presence of nonmetallic F, Cl and OH. Gong [27] demonstrated that hydroxyls play a critical role in the formation and propagation of oxygen vacancy clusters (VCs), and the neighboring hydroxyls could stabilize the thermodynamically unstable VCs. Briefly, the theoretical calculations suggest that surface chemical groups such as hydroxyls would change the chemical stability of surface defects of  $\text{CeO}_2$  catalysts, which possibly affects the catalytic performance.

Due to the importance of the surface properties in interfacial reaction processes, a survey of  $\text{CeO}_2$  with different exposing lattice planes in the Fenton-like applications is carried out in this work, which is expected to provide experimental references for researchers to understand the influence of the surface properties in the heterogeneous Fenton-like applications of  $\text{CeO}_2$ . The adsorption properties of Orange II (AO7) on  $\text{CeO}_2$  with different exposing crystal facets are emphatically investigated, including adsorptive kinetics and apparent adsorption enthalpy. Moreover, the influence of surface hydroxyl content for  $\text{CeO}_2$ -based Fenton-like degradation reactivity will also be taken into account in this work. Besides, the reactivity between  $\text{H}_2\text{O}_2$  molecules and surface cerium ions is also discussed.

## 2. Experimental

### 2.1. Reagents and materials

$\text{Ce}(\text{NO}_3)_3 \cdot 6\text{H}_2\text{O}$  were purchased from Shanghai Sinopharm Chemical Reagent.  $\text{NH}_3 \cdot \text{H}_2\text{O}$  (28%) and  $\text{H}_2\text{O}_2$  (30%) were supplied by Shanghai Lingfeng Chemical Reagent. AO7 dye was obtained from Acros. All reagents were of analytical grade and used as received without further purification. Ultra-pure water ( $18\text{ M}\Omega/\text{cm}$ ) was used throughout the experiments.

### 2.2. Material synthesis

The synthesis of ceria nanocatalysts with specific shapes has been described in previous reports [18,28].  $\text{CeO}_2$  of special crystals were synthesized by a solution-based hydrothermal method as follows. Typically, 2.891 g  $\text{Ce}(\text{NO}_3)_3 \cdot 6\text{H}_2\text{O}$  was dissolved in 40 mL water. Then NaOH aqueous solution (5.0 mol/L, 40 mL) was added dropwise into the cerium salt solution under stirring at room temperature. The mixed solution was adequately stirred for an additional 60 min and then transferred into a 100 mL Teflon container. The Teflon container was tightly sealed and hydrothermally treated in a stainless-steel autoclave at different temperatures for 24 h. According to the literature reports [28], hydrothermal temperature would determine the morphology of the as-prepared  $\text{CeO}_2$  materials, that is, rod shape (labeled as *r*) at 100 °C and cube shape (labeled as *c*) at 180 °C. After cooling, the as-obtained precipitates were collected, washed and dried in vacuum drying oven at 80 °C overnight. The dried yellow powders were then calcined in air at different temperatures (*T*) for 4.0 h. According to their shape, the samples are labeled as *r*-T and *c*-T, respectively.

In addition,  $\text{CeO}_2$  nanoparticles were also prepared by a traditional deposition precipitation method:  $\text{NH}_3 \cdot \text{H}_2\text{O}$  (6.0 mL, 28%) was

added dropwise to a  $\text{Ce}(\text{NO}_3)_3$  solution (0.1 mol/L, 100 mL) with vigorous stirring to form a yellowish suspension. The suspension was stirred continuously for 2 h at 40 °C followed by aging for 12 h. The resulting purple precipitate was collected by centrifugation, washed several times with water, and dried at 60 °C under vacuum for 12 h. After grinding, the precipitate was heated to 500 °C at 2 °C/min and held at this temperature in air for 4 h to obtain  $\text{CeO}_2$  powders, which is labeled as DP in this work.

### 2.3. Fenton-like degradation of AO7

The activity of different catalysts was evaluated with the degradation of AO7. Generally, 0.025 g catalyst powder was added into a quartz tube containing 50 mL AO7 (40 mg/L) aqueous solution. The suspension was stirred in the dark for 1.0 h to ensure the establishment of an adsorption-desorption equilibrium. Then  $\text{H}_2\text{O}_2$  solution was added to reach a  $\text{H}_2\text{O}_2$  concentration of 20 mM. At the given time intervals, samples (3.0 mL) were taken from the mixture and immediately centrifuged. The concentration of dye in supernatant was analyzed by recording its variation of the absorbance at 484 nm by utilizing a UV-vis spectrophotometer (Shimadzu UV-2600).

### 2.4. AO7 adsorption studies

The influences of initial AO7 concentration on the dye adsorption were investigated at 40 °C. In study of adsorption kinetics, AO7 aqueous solutions (50 mL) of different concentrations were mixed with 0.025 g catalyst in batch experiments. At the given time intervals, samples (2.0 mL) were taken from the mixture and immediately filtered with a micro-filtration membrane (0.22  $\mu\text{m}$ ) to remove the catalyst powders. The filtrate was analyzed by recording its absorbance at 484 nm.

### 2.5. Methods of analysis

Raman measurements were performed at room temperature using a Renishaw Via+ Reflex Raman spectrometer with the excitation light of 532 nm. The UV-vis diffuse reflectance spectra (DRS) of catalysts were recorded by a UV-vis spectrophotometer (Shimadzu UV-2600). XRD analysis of the catalysts was carried out with Rigaku Ultima IV apparatus using  $\text{Cu K}\alpha$  radiation ( $\lambda = 0.15406\text{ nm}$ ) and a graphite monochromator at room temperature, operated at 40 kV and 40 mA. The BET specific surface area ( $S_{\text{BET}}$ ) and BJH pore size distribution were determined by nitrogen adsorption at 77.3 K (Micromeritics ASAP 2020). The morphologies of catalysts were obtained by a transmission electron microscope (TEM, JEM-2100). A Perkin-Elmer PHI 5000C ESCA system with  $\text{Al K}\alpha$  radiation operated at 250 W was utilized for X-ray photoelectron spectroscopy (XPS) measurement to study the surface chemical constitution of the samples.

## 3. Results and discussion

### 3.1. Physical properties of $\text{CeO}_2$ nanomaterials

The phase purity and crystal structure of the as-prepared  $\text{CeO}_2$  nanorods and nanocubes are characterized by XRD patterns (Fig. 1). All samples display typical XRD patterns of cubic  $\text{CeO}_2$  (fluorite structure, JCPDS 34-0349). The cubes exhibit sharper XRD peaks than the rods, indicating higher crystallinities of the cubes. Meanwhile, the XRD peaks become more acute after calcined at higher temperatures both for rods and cubes, implying the increase of crystallinity under calcination. Their BET specific surface areas (Table S1) of the rods decrease slightly when calcined below 400 °C, and then significantly after calcined at 500 °C, which can be attributed to the sintering, considering its slightly increased grain size.

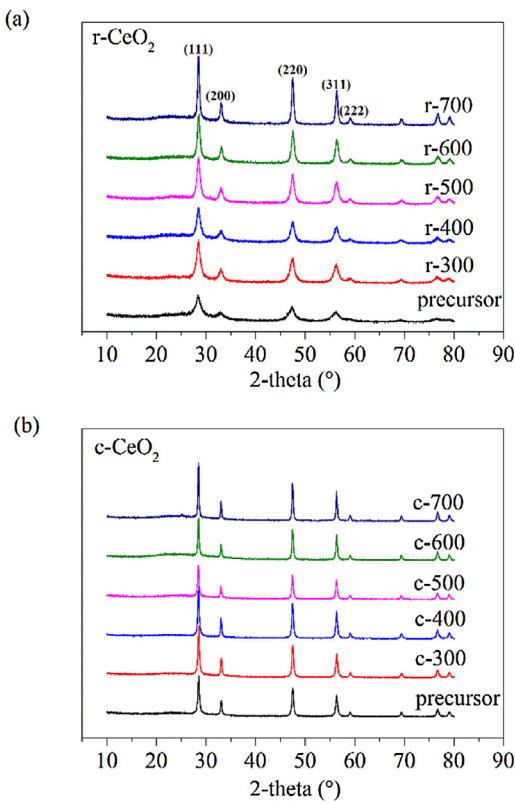


Fig. 1. XRD patterns of (a) CeO<sub>2</sub> rods and (b) CeO<sub>2</sub> cubes.

The previous works have reported that the nanorods mainly expose {110} and {100} facets while cubes expose their {100} facet [28]. Fig. 2a and b exhibits the TEM image of r-precursor and r-500. Generally, characteristic interplanar spacings of 0.32, 0.28, and 0.19 nm correspond to {111}, {200}, and {220} planes for CeO<sub>2</sub>, respectively. The calcined rods preserve well the rod-like shape; both the r-precursor and the r-500 CeO<sub>2</sub>s show a 1D growth structure with a preferred growth direction along [110], which enclosed by {220} planes (Fig. 2c). Thermal treatment seems not change the morphology as well as the exposed facets of CeO<sub>2</sub> rods. Similarly, the morphology of nanocubes is also unchanged under calcination as shown in Fig. 2d and 2e. The TEM image of nanocubes (Fig. 2f) displays the clear {200} lattice fringe with a characteristic interplanar spacing of 0.27 nm. However, the size of the CeO<sub>2</sub> grains begins to increase when calcined under 500 °C. Considering that the morphology change of the grains would occur when calcined above 500 °C, for instance, Mai et al. [28] revealed that the exposed facets of CeO<sub>2</sub> nanorods changed as the calcination temperature enhanced from 500 °C to 700 °C, the samples calcined above 500 °C were not taken into consideration in this work.

Nanorods and nanocubes in this work expose two characteristic facets of CeO<sub>2</sub>, which gives us an opportunity to investigate the reactivity of each particular facet in the interfacial catalytic reactions. Hereinafter, the Fenton-like reactivity of CeO<sub>2</sub> nanorods and nanocubes is carefully investigated. For a reference, CeO<sub>2</sub> nanoparticles (DP) of truncated octahedral obtained by precipitation method (Fig. S1) was also used, which mainly exposes {111} facets, as they constitute the most stable low-index surface of ceria. DP CeO<sub>2</sub> also display a typical cubic fluorite structure (JCPDS 34-0349), with a specific surface area of 63.7 m<sup>2</sup>/g.

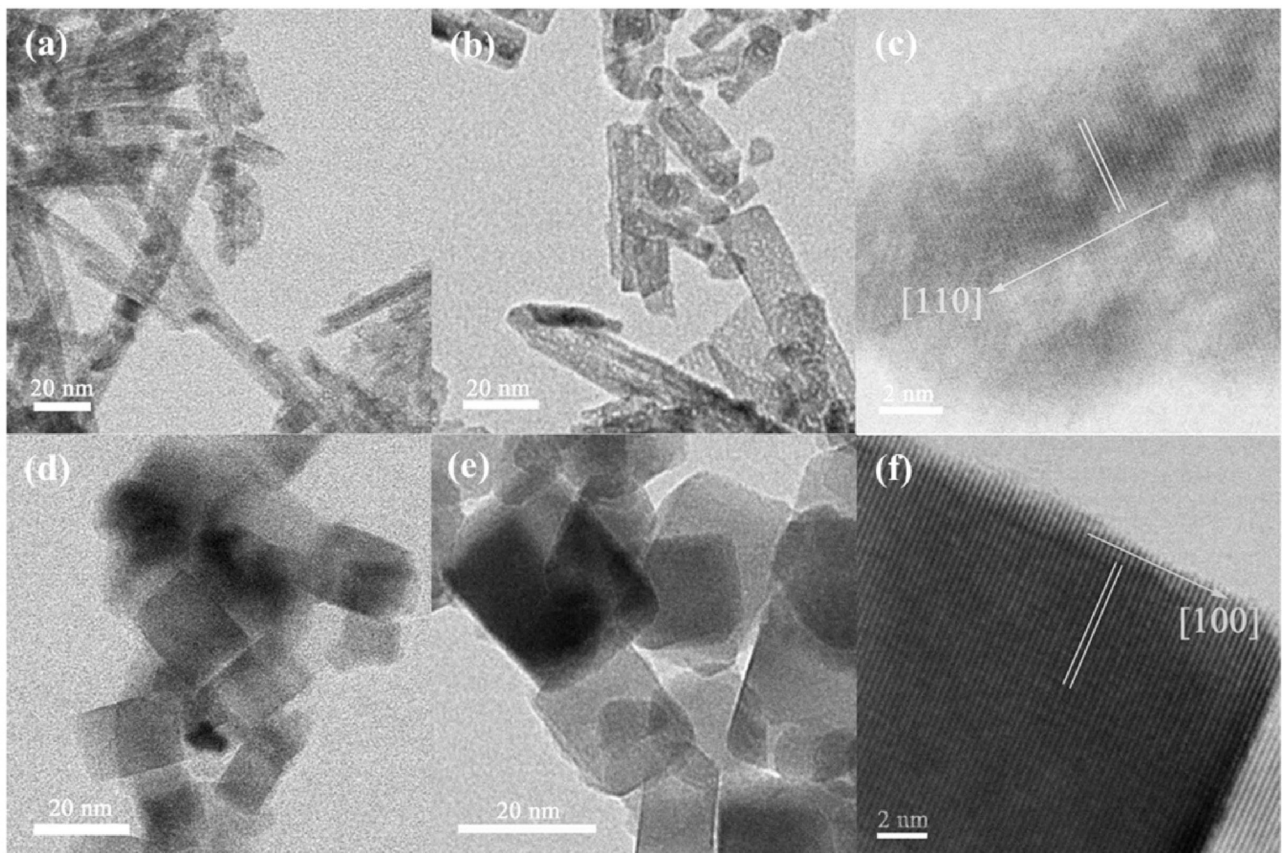
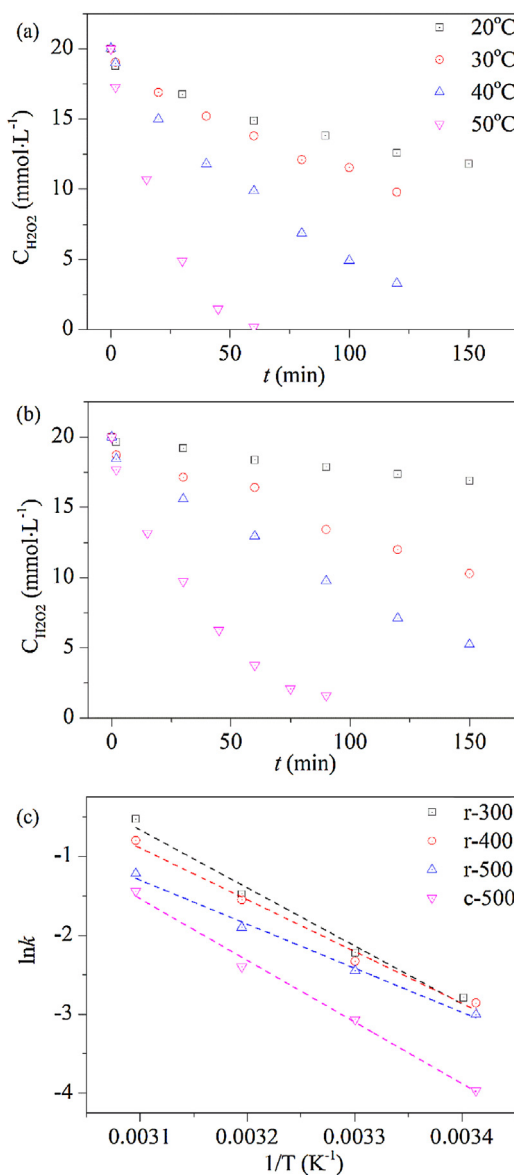


Fig. 2. TEM and HRTEM images of CeO<sub>2</sub> nanocrystals: (a) r-precursor; (b-c) r-500; (d) c-precursor; (e-f) c-500.



**Fig. 3.**  $\text{H}_2\text{O}_2$  decomposition process of (a) r-500 and (b) c-500; (c) Apparent Arrhenius plot of different samples.

### 3.2. Decomposition of $\text{H}_2\text{O}_2$ in a simple $\text{CeO}_2$ - $\text{H}_2\text{O}_2$ system

In order to understand the Fenton-like reactivity on  $\text{CeO}_2$  of different morphologies, the  $\text{H}_2\text{O}_2$  concentration changes towards  $\text{CeO}_2$  were carefully investigated in the absence of other substances. The decomposition processes of  $\text{H}_2\text{O}_2$  on r-500 and c-500 are shown in Fig. 3a and b, while those on r-300 and r-400 are shown in Fig. S2. The  $\text{H}_2\text{O}_2$  concentration experiences an obvious decline in the first several minutes as soon as  $\text{H}_2\text{O}_2$  was added into the solution, which can be attributed to a rapid adsorption of  $\text{H}_2\text{O}_2$ . In the first 2 min, the  $\text{H}_2\text{O}_2$  decrement follows the order of r-300 > r-400 > r-500, implies that  $\text{H}_2\text{O}_2$  shows the stronger adsorption over r-300. The  $\text{H}_2\text{O}_2$  decay kinetics can be well described by a zero-order kinetics for both r-500 and c-500, which is accelerated at higher temperatures. The  $\text{H}_2\text{O}_2$  decomposition rate constants of r-300, r-400, r-500 and c-500 at 40 °C are calculated as 0.228, 0.212, 0.157 and 0.091 mol/L min<sup>-1</sup>, respectively. The variations in rate constant can be ascribed to the changes in specific surface area, as well as in the surface chemical states. Though the cerium element at the exposed surface of  $\text{CeO}_2$  mainly presents as

**Table 1**  
O(1s) peak parameters for different materials.

States of Oxygen		Percent (%)			
Species	B. E. (eV)	r-300	r-400	r-500	c-500
Ce(IV)-O	529.20	71.9	79.0	84.0	82.9
Ce(III)-O <sup>a</sup>	530.60	7.3	4.7	5.5	2.0
$\text{OH}^-$	531.60	20.8	16.3	10.5	15.1

<sup>a</sup> one oxygen vacancy creates two Ce(III) species.

$\text{Ce}(\text{IV})$ , the  $\text{Ce}(\text{III})$  state of cerium, accompanied with the oxygen vacancy, is presumed to be the reactive site for catalyzing  $\text{H}_2\text{O}_2$  [29]. The active site density of  $\text{CeO}_2$ , would be changed during the calcinations (confirmed with XPS and Raman spectra hereinafter), and has a significant impact on the  $\text{H}_2\text{O}_2$  decomposition rate.

As shown in Fig. 3c, apparent activation energies ( $E_a$ ) for  $\text{H}_2\text{O}_2$  decomposition with r-300, r-400, r-500 and c-500 are calculated to be 61.0, 54.5, 46.3 and 64.8 kJ/mol with Arrhenius Equation, respectively. As for reference, the activation energy for  $\text{H}_2\text{O}_2$  self-decomposition is known as 75.3 kJ/mol.  $E_a$  decreases with enhancing the calcination temperature, and gives the lowest value over r-500 among all samples. Academically, the value of  $E_a$  should be predominantly determined by the Ce(III)/Ce(IV) redox cycle, with which the adsorption and decomposition of  $\text{H}_2\text{O}_2$  are achieved. As  $\text{CeO}_2$  is less likely to releasing lattice O atom at ambient condition, the oxygen vacancy can not be on-site produced during the Fenton-like reaction. Hence, the decomposition of  $\text{H}_2\text{O}_2$  is proposed mainly occurs at the oxygen vacancy sites. According to the DFT calculation, the surface hydroxyl can lower surface energy and stabilize the surface by orbital hybridization with the surface Ce and O atoms; in this way, oxygen vacancy can be stabilized with the adjacent surface hydroxyl [26,27]. Since the thermal treatment significantly reduces the amount of surface hydroxyl groups on  $\text{CeO}_2$  (Table 1).  $\text{CeO}_2$  with relatively higher density of oxygen vacancies (r-300 here) gives a higher  $\text{H}_2\text{O}_2$  decomposition activity. Further, it is relatively more temperature-sensitive for  $\text{H}_2\text{O}_2$  decomposition and rises faster when increasing the reaction temperature.

XPS measurement was used to evaluate the relative concentration of Ce(III) on the surface of  $\text{CeO}_2$  with different morphologies. Fig. 4 shows the  $\text{Ce}_{3d}$  fine XPS spectra of r-500 and c-500. The deconvolution of  $\text{Ce}_{3d}$  fine XPS spectra could be labeled as two pairs of doublets ( $v_0/u_0$  and  $v'/u'$ ) assigned to Ce(III) and three pairs of doublets ( $v/u$ ,  $v''/u''$  and  $v'''/u'''$ ) assigned to Ce(IV). For each doublet, v and u refer to  $3d_{5/2}$  and  $3d_{3/2}$  spin-orbit component of cerium ion, respectively [11,30,31]. The relative concentration of Ce(III) could be calculated from the integrated areas of deconvoluted peaks according to Eq. (1):

$$[\text{Ce}^{3+}] = \frac{A_{v_0} + A_{v'} + A_{u_0} + A_{u'}}{A_{v_0} + A_{v'} + A_{u_0} + A_{u'} + A_v + A_{v''} + A_{v'''} + A_u + A_{u''} + A_{u'''}} \times 100\% \quad (1)$$

According to Eq. (1), the Ce(III) contents of r-300, r-400, r-500 and c-500 are calculated as 15.4%, 14.9%, 11.2% and 16.9%, respectively. Accordingly, increase of calcination temperature (from 300 to 500 °C) results in a little decline in the content of trivalent cerium ions (Ce(III)). Wang [32] reported that oxygen vacancies were oxidized at elevated calcination temperature from 180 °C to 500 °C.

Raman spectroscopy is widely used in chemical analysis, since vibrational information is specific to the chemical bonds. Fig. 5a shows that  $\text{CeO}_2$  presents a strong band at 463 cm<sup>-1</sup>, which assigned to the  $F_{2g}$  vibration mode of the O atoms around each  $\text{Ce}(\text{IV})$  ion [32,33]. The weak band at 1172 cm<sup>-1</sup> is attributed to second-order phonon mode of fluorite structure, while the band at 593 cm<sup>-1</sup> is associated to the oxygen vacancies and widely observed in  $\text{CeO}_{2-x}$ . Generally, by comparing the ratio of Raman peak intensity at 593 cm<sup>-1</sup> to that at 463 cm<sup>-1</sup> (recorded as

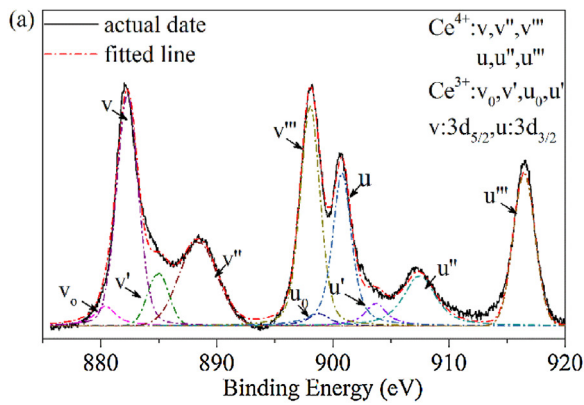


Fig. 4. Fine XPS spectra of  $\text{Ce}_{3d}$  for (a) r-500 and (b) c-500.

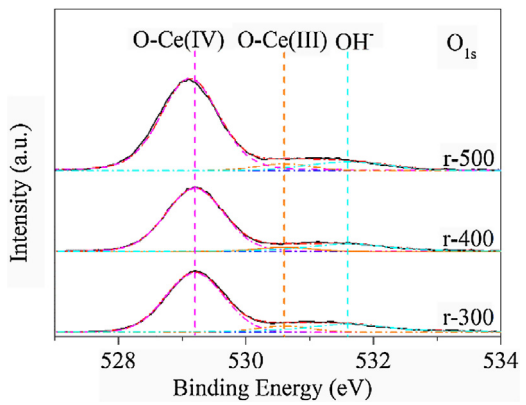


Fig. 6. Fine XPS spectra of  $\text{O } 1s$  for  $\text{CeO}_2$  nanorods.

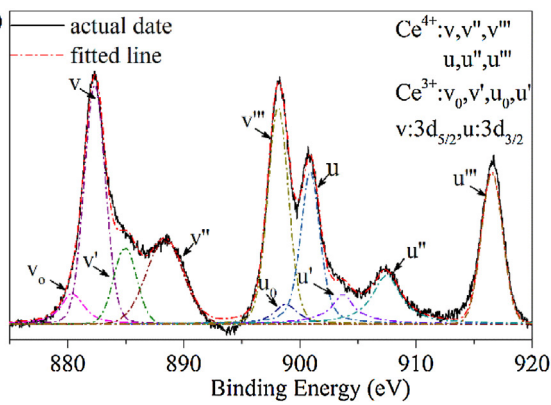


Fig. 4. Fine XPS spectra of  $\text{Ce}_{3d}$  for (a) r-500 and (b) c-500.

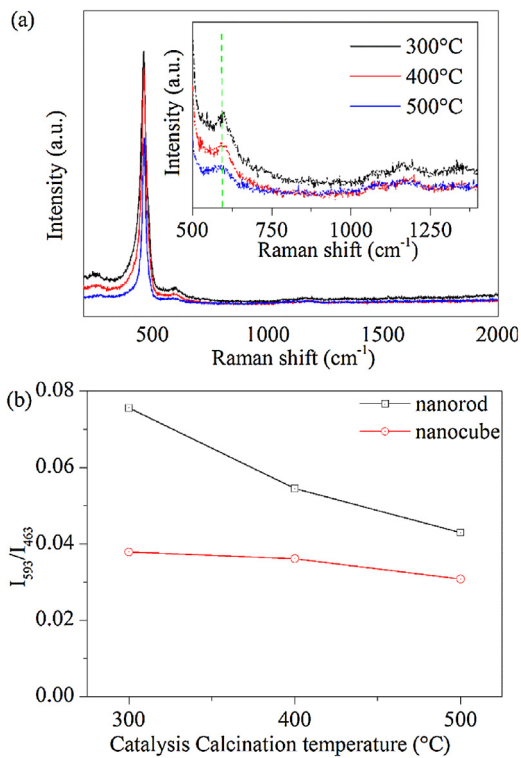


Fig. 5. (a) Raman spectra of  $\text{CeO}_2$  nanorods, and (b) the corresponding  $I_{593}/I_{463}$  ratios of nanorods and nanocubes.

$I_{593}/I_{463}$ ), the relative concentration of oxygen vacancy in  $\text{CeO}_2$  can be estimated. Fig. 5b shows that the value of  $I_{593}/I_{463}$ , the relative concentration of bulk oxygen vacancy in  $\text{CeO}_2$ , decreases with the increase of calcination temperature for both nanorods and nanocubes. It means that the thermal treatment eliminates part of oxygen vacancies in  $\text{CeO}_2$ , which is consistent with the XPS spectra results above (note that one oxygen vacancy creates two  $\text{Ce}(\text{III})$  species). According to the XPS and Raman results, it is presumed that the specific decomposition rate constants of  $\text{H}_2\text{O}_2$  should be exhibited in an order of  $r-300 > r-400 > r-500$  (See Fig. 9b hereinafter), due to the corresponding  $\text{Ce}(\text{III})$  concentrations. In other words, the enhanced  $\text{H}_2\text{O}_2$  decomposition rate constant ( $k$ ) could be ascribed to a larger surface area and a higher  $\text{Ce}(\text{III})$  concentration.

Fig. 6 presents the  $\text{O } 1s$  fine XPS spectra of  $\text{CeO}_2$  nanorods, which can be deconvoluted into three peaks at 529.2, 530.60 and 531.60 eV, which represent the three different states of oxygen that chemically bond with  $\text{Ce}(\text{IV})$ ,  $\text{Ce}(\text{III})$  and  $\text{H}$ , respectively [30,34–36]. Molecular water gives  $\text{O } 1s$  binding energy signals around 532 eV [37], which is not identified in the XPS spectra. According to the simulation calculation based on DFT-GGA+U, Molinari [38] predicted that when considering the presence of  $\text{Ce}(\text{III})$ , hydroxyl group desorbs at higher temperature (400–600 K) compared to associatively adsorbed water. Desorption temperature shows a marked shift toward high temperature when the oxides moving from stoichiometric to reduced surfaces. Mullins [37] reported that the dissociated hydroxyl group desorbs as water on the reduced  $\text{CeO}_{2-x}$  (100) facet over a broad range from 180 to 700 K. Table 1 summarizes the calculated contents of the surface oxygen species of various  $\text{CeO}_2$  nanorods. The r-300 has the most abundant (20.8%) content of hydroxyl group. The hydroxyl group content decreases significantly with the enhanced calcination temperature, gives a value of 10.5% after calcined at 500 °C.

Wu [27] reported that the thermodynamically unstable oxygen vacancy clusters can be significantly stabilized in presence of adjacent hydroxyls through lowering their surface energies. Along with the variation of surface  $\text{Ce}(\text{III})$  content, the surface hydroxyl content dramatically reduced with the enhanced thermal treatment process, which should play a role in  $\text{H}_2\text{O}_2$  adsorption and Fenton-like decomposition process [39].

Generally, brownish interfacial peroxide-like species ( $=\text{Ce}(\text{III})-\text{O}_2\text{H}^-$ ) generate in  $\text{CeO}_2/\text{H}_2\text{O}_2$  system via the complexation of  $\text{H}_2\text{O}_2$  with  $\text{Ce}(\text{III})$ . The interfacial peroxide-like species are thought to be the active oxygen species for the decomposition of  $\text{H}_2\text{O}_2$  or degradation of AO7. A  $\text{Ce}(\text{III})/\text{Ce}(\text{IV})$  redox cycle plays a significant role in this process [4,11]. Wang [40] has reported that the regeneration of  $\text{Ce}(\text{III})$  (the reduction of  $\text{Ce}(\text{IV})$ ) with excess  $\text{H}_2\text{O}_2$  would be the rate-determining step in the decomposition process of hydrogen

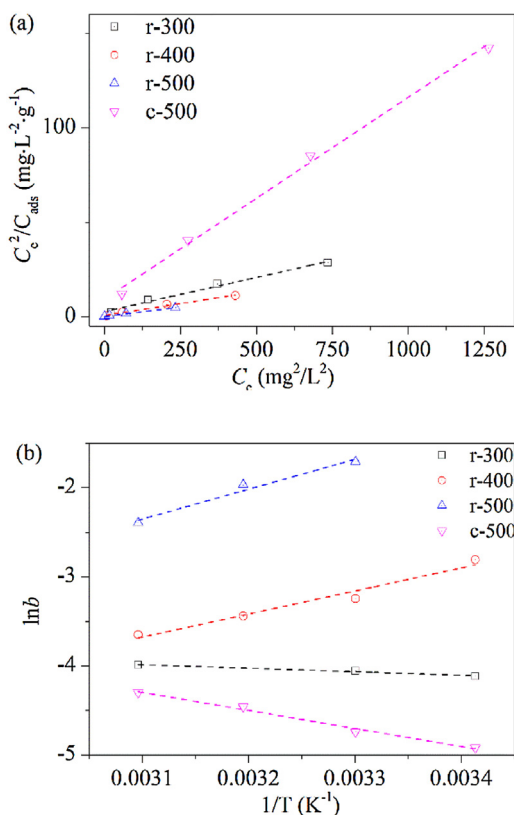


**Fig. 7.** (a) Langmuir model linear equations for the adsorption of AO7 on different samples at 40 °C. (b) The dependence of the adsorption coefficient on temperature for different samples at pH 6.55 ± 0.05.

peroxide; i.e., the  $\text{H}_2\text{O}_2$  decomposition rate greatly depends on the reducibility of  $\text{CeO}_2$ . The surface energies of the pure {111}, {110} and {100} facets are calculated as 0.68, 1.01 and 1.41 J m<sup>-2</sup>, [41] respectively, while their corresponding vacancy formation energies are 2.60, 1.99 and 2.27 eV. Academically, {110} facet has the lowest vacancy formation energy for  $\text{CeO}_2$ , that is, more readily to be reduced. Therefore, the reason of a higher  $E_a$  for  $\text{H}_2\text{O}_2$  decomposition with nanocube (c-500) than that with nanorod can be related to its exposed facets. In other words, the regeneration of Ce(III) (oxygen vacancy formation) would be easier on  $\text{CeO}_2$  nanorods than on nanocubes, which facilitates the  $\text{CeO}_2$ -based Fenton-like degradation process [15,42,43]. Besides, the  $E_a$  values for  $\text{H}_2\text{O}_2$  decomposition decrease for the rods with the enhanced calcination temperature, implies the reducing of oxygen vacancy formation energy in well crystallized (110) facet.

### 3.3. AO7 adsorption isotherm and kinetics on $\text{CeO}_2$

The adsorption of dye on the catalyst plays an important role in its Fenton-like degradation process [15]. For better understanding the Fenton-like degradation details of AO7, the adsorption of AO7 on  $\text{CeO}_2$  catalysts is surveyed. As shown in Fig. 7a, the adsorption behaviors of AO7 can be evaluated with Langmuir isothermal secondary adsorption equation as follows.

$$C_{ads} = C_{ads}^* \cdot \frac{bC_e^2}{1 + bC^2 e} \text{ or } \theta_{AO7} = \frac{bC_e^2}{1 + bC^2 e} \quad (2)$$

$$C_e^2/C_{ads} = 1/C_{ads}^* b + C_e^2/C_{ads}^* \quad (3)$$

In the equations,  $C_e$  (mg/L) represents the adsorption equilibrium concentration in the solution,  $b$  stands for the adsorption coefficient,  $C_{ads}$  (mg/g) and  $C_{ads}^*$  (mg/g) indicate the adsorption amounts

of AO7 onto  $\text{CeO}_2$  at time  $t$  and equilibrium, respectively, while  $\theta_{AO7}$  stands for the surface coverage of AO7 on the catalyst surface. Fig. 7a shows that the saturated adsorption amounts of AO7 on the catalysts are 27.8, 40.1, 50.5 and 9.4 mg/g for r-300, r-400, r-500 and c-500, respectively, while the corresponding adsorption coefficients ( $b$ ) are estimated as 0.013, 0.032, 0.140 and 0.012. The differences of adsorption should be related to the specific surface area variation, as well as other surface factors such as surface hydroxyl coverage [39], for the  $\text{CeO}_2$  samples.

Generally, Ce(IV) is six-fold coordinated on the {110} and {100} facets and seven-fold coordinated on  $\text{CeO}_2$  {111} facet which means that the Ce(IV) sites on the surface of rods and cubes would exhibit stronger acid strengths and bind adsorbates more strongly than those on DP  $\text{CeO}_2$  with exposed {111} facet [44]. However, the {100} facet is academically terminated with oxygen; considering the relatively large volume of AO7 molecules, it is difficult to form on-top adsorbate on the Ce(IV) site due to the steric hindrance of the surface oxygen [45]. Experimentally, the equilibrium adsorption amounts for DP, r-500, c-500 are 0.444, 0.691 and 0.366 mg/m<sup>2</sup> at an initial AO7 concentration of 40 mg/L at 40 °C, which partially corresponds the surface characteristics of the exposed facets of above  $\text{CeO}_2$  materials. According to the Gibbs function calculation, the apparent adsorption enthalpy ( $\Delta H_{app}$ ) of AO7 can be calculated. As shown in Fig. 7b, the calculated  $\Delta H_{app}$  for r-300, r-400, r-500 and c-500 are 3.25, -21.54, -27.90 and 16.87 kJ/mol, respectively. The AO7 adsorption on r-300 is an endothermic process, while that on r-400 and r-500 is an exothermic process. Furthermore, the c-500 present a major difference relative to r-500, which is possibly due to the effect of steric hindrance of the surface oxygen on {100} facet and implies that the AO7 adsorption process on  $\text{CeO}_2$  is much surface-structure-sensitive.

The adsorption of AO7 is significantly improved for  $\text{CeO}_2$  nanorods at the elevated thermal temperature, which is just opposite to the adsorption of  $\text{H}_2\text{O}_2$  shown in Fig. 3 and Fig. S2. Generally, decrease of oxygen vacancy concentration could be adverse to the AO7 adsorption and Fenton-like degradation rate [4,11,15]. However, the experimental results did not agree with such a conjecture, which may be associated with the exposure condition of the cerium ions at the surface. It is reported that the O terminal is removed after thermal treatment for the {100} facet, which should contribute much to the AO7 adsorption due to the exposure increase of cerium ions [46]. Further, the density of surface hydroxyl group is also proposed playing an important role for the AO7 adsorption. The hydroxyl is presented as a coordinator to the surface cerium ion, which contributes a coordination number increase to cerium ion and may block the adsorption of AO7. That is, surface hydroxyl is also negative for AO7 Fenton-like degradation due to its site-blocking effect [47,48]. In a word, the changes in the amount of exposed cerium ions and the density of the surface hydroxyl should be responsible for the AO7 molecule adsorption enhancement on  $\text{CeO}_2$ .

### 3.4. Fenton-like degradation of AO7 in $\text{CeO}_2$ - $\text{H}_2\text{O}_2$ system

It is previously reported that the surface peroxide formed by a reaction between adsorbed  $\text{H}_2\text{O}_2$  molecules and surface cerium ion, induces an intermolecular rearrangement with the neighboring adsorbed organic molecules to achieve the degradation of substances such as salicylic acid and sodium dodecylbenzenesulfonate [4,11,15,49].

Fig. 8a presents the degradation of AO7 over different samples in the neutral environment in dark. Typical UV-vis absorbance and pH value evolutions of the AO7 solution during the Fenton-like reaction are shown in Figs. S3&S4. The oxidation of AO7 is negligible with  $\text{H}_2\text{O}_2$  in the absence of catalyst. After the initial adsorption equilibrium, AO7 adsorbs greatly on the surface of  $\text{CeO}_2$  catalyst.

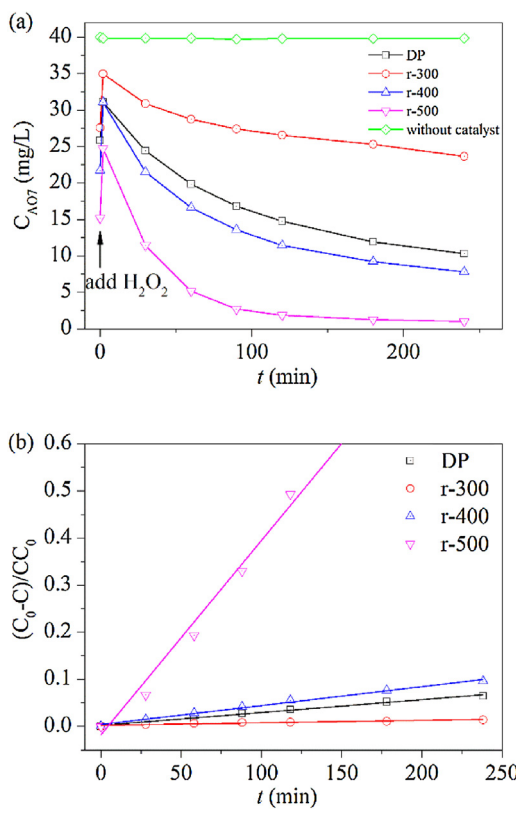


**Fig. 8.** (a) Adsorption and degradation of AO7 in CeO<sub>2</sub>-H<sub>2</sub>O<sub>2</sub> system over different nanorods. (b) The relevant degradation kinetic processes of AO7. [CeO<sub>2</sub>]=0.5 g/L, [AO7]=40 mg/L, [H<sub>2</sub>O<sub>2</sub>]=20 mM, pH=6.55±0.05.

The AO7 adsorption amount over r-500 was apparently higher than other samples. The addition of H<sub>2</sub>O<sub>2</sub> causes a quick and obvious desorption of AO7 attributed to a competitive adsorption occurred on the catalyst surface [15]. The kinetics of AO7 degradation can be described by pseudo-second order kinetics (Fig. 8b) and the degradation rate of AO7 reaches over 95% after 2 h over r-500. The calculated degradation rate constants of AO7 are  $2.7 \times 10^{-4}$ ,  $0.5 \times 10^{-4}$ ,  $4.0 \times 10^{-4}$  and  $4.2 \times 10^{-3} \text{ L g}^{-1} \text{ min}^{-1}$ , respectively for sample DP, r-300, r-400 and r-500. The AO7 degradation rate of r-500 is much higher than other samples. As previously reported [15], the AO7 degradation in CeO<sub>2</sub>-H<sub>2</sub>O<sub>2</sub> system could be described as an interfacial reaction of adsorbed dye molecules with active oxygen species in-situ generated on CeO<sub>2</sub> surface, which presents a second-order reaction followed the Langmuir-Hinshelwood mechanism (Eq. (4)).

$$r = k[\text{O}_{\text{surf}}][\text{L}_{\text{ads}}] \quad (4)$$

Here O<sub>surf</sub> refers to the interfacial peroxide species generated from the surface complexation of H<sub>2</sub>O<sub>2</sub> with cerium ion, L<sub>ads</sub> is the adsorbed dye molecules, while k is the theoretical reaction rate constant. Generally, the interfacial peroxide species undergoes a homolytic cleavage of the O–O bond to generate hydroxyl radical to attack the adjacent adsorbed substances (AO7, H<sub>2</sub>O<sub>2</sub> et.al) via the oxidation of Ce(III). The as-formed Ce(IV) then coordinates with HO<sub>2</sub><sup>–</sup> and is reduced to Ce(III). The recovered catalytic sites are able to form surface peroxide species and start a next catalytic cycle. Although r-500 exhibits a relatively smaller surface area and a lower Ce(III) concentration, it also owns a reduced oxygen vacancy formation energy, which benefits the reduction of Ce<sup>4+</sup> and remedies the weaknesses of smaller surface area and lower active site concentration at room temperature. Therefore, the generation rate of interfacial peroxide species for r-500 is almost equal to those for

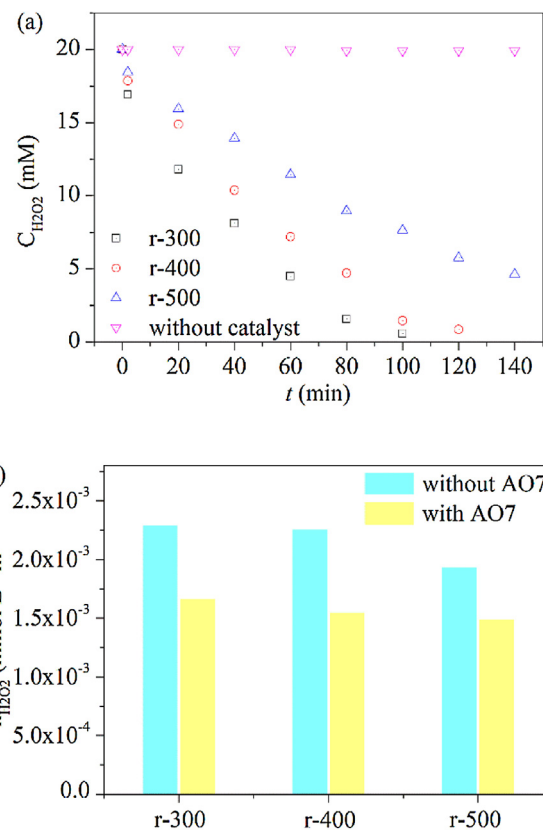


**Fig. 9.** (a) The H<sub>2</sub>O<sub>2</sub> decomposition process over CeO<sub>2</sub> nanorods. (b) The contrast of H<sub>2</sub>O<sub>2</sub> decomposition rate per unit area with and without the addition of AO7. [CeO<sub>2</sub>]=0.5 g/L, [AO7]=40 mg/L, [H<sub>2</sub>O<sub>2</sub>]=20 mM, pH=6.55±0.05.

r-300 and r-400 at a relatively low temperature (Fig. 3c). What's more, as previously discussed, the enhanced calcination temperature could enhance the adsorption of AO7 molecules on nanorods. Thus, AO7 molecules have a relatively elevated probability to be attacked by the adjacent peroxide species, then oxidized into small molecules.

To further understanding the Fenton-like reaction kinetics in CeO<sub>2</sub>-H<sub>2</sub>O<sub>2</sub>/AO7 system, the concentration variation of H<sub>2</sub>O<sub>2</sub> was also monitored. Fig. 9 shows the H<sub>2</sub>O<sub>2</sub> decay kinetics and the specific decomposition rates per unit area of H<sub>2</sub>O<sub>2</sub> with nanorods. No H<sub>2</sub>O<sub>2</sub> decomposition is observed in the absence of catalyst. The H<sub>2</sub>O<sub>2</sub> decay kinetics in the presence of catalyst can still be described by zero-order kinetics and the differences in H<sub>2</sub>O<sub>2</sub> consumption among nanorod samples are slight after addition of AO7, although r-300 shows relatively higher H<sub>2</sub>O<sub>2</sub> consumption rate than other samples. It suggests that the generation or consumption rates of surface peroxide species have little differences at 40 °C. The decreased H<sub>2</sub>O<sub>2</sub> consumption after addition of AO7 could be ascribed to the competitive adsorption and reaction over active sites between H<sub>2</sub>O<sub>2</sub> and AO7 molecules. In term of different adsorption models, the H<sub>2</sub>O<sub>2</sub> consumption and AO7 degradation present different regular changes over different heat-treatment nanorod samples.

Fig. 10 presents that the adsorption and degradation of AO7 in CeO<sub>2</sub>-H<sub>2</sub>O<sub>2</sub> system over different nanocubes. Similarly, the AO7 adsorption amount on catalysts increases with the elevated calcination temperature, as thermal treatment contributes more surface exposed cerium ions. However, the degradation rates of AO7 with nanocubes are much lower than those with nanorods. The derated performance of nanocubes can be partly related to their smaller specific surface areas. Another reason should be ascribed to the relatively higher formation energy of oxygen vacancy for (100) facet,

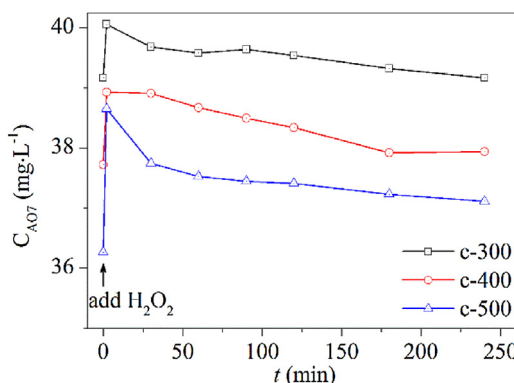


**Fig. 10.** Adsorption and degradation of AO7 in  $\text{CeO}_2$ - $\text{H}_2\text{O}_2$  system over nanocubes.

which results in a debilitated  $\text{Ce}(\text{III})/\text{Ce}(\text{IV})$  redox cycle, as well as much slower self-decomposition rates of  $\text{H}_2\text{O}_2$  with  $\text{CeO}_2$  (Fig. 3) at room temperature.

#### 4. Conclusion

$\text{CeO}_2$  nanorods and nanocubes with well-defined planes were successfully synthesized with a solution-based hydrothermal method. A higher  $E_a$  for  $\text{H}_2\text{O}_2$  decomposition with nanocube (c-500) than that with nanorod could be related to the low oxygen vacancy formation energy on  $\{110\}$  facet, indicated that the interface peroxide species are easier to generate on exposed  $\{110\}$  facet. The adsorption of AO7 over  $\text{CeO}_2$  is found to be dependent on the exposed facets. The nanocubes present weak AO7 adsorption property, leading to declined Fenton-like degradation activities for AO7. For the nanorods, the increased calcination temperature up to 500 °C induces a decreased amount of surface hydroxyls and reduced coordination status of surface Ce cations, and thus greatly promotes the AO7 adsorption capacity on  $\text{CeO}_2$ . Meanwhile, the decreased oxygen vacancy formation energy accelerates the formation of interface peroxide species, remedying the relatively low concentration of oxygen vacancies for the application of r-500 in Fenton-like reaction. Consequently, r-500 presents the highest AO7 Fenton-like degradation rate. Exposed  $\{110\}$  and  $\{100\}$  facets play very important roles in the Fenton-like reaction with  $\text{CeO}_2$ , that is, Exposing particular crystal facet can be an effective strategy to optimize the reactivity of catalysts in many applications.

#### Acknowledgement

This work was supported by the National Nature Science Foundations of China (21177039, 21677049).

#### Appendix A. Supplementary data

Supplementary data associated with this article can be found, in the online version, at <http://dx.doi.org/10.1016/j.apcatb.2017.05.068>.

#### References

- [1] E. Neyens, J. Baeyens, J. Hazard. Mater. 98 (2003) 33–50.
- [2] A.D. Bokare, W. Choi, J. Hazard. Mater. 275 (2014) 121–135.
- [3] H.W. Liang, H.Q. Sun, A. Patel, P. Shukla, Z.H. Zhu, S.B. Wang, Appl. Catal. B 127 (2012) 330–335.
- [4] P. Ji, L. Wang, F. Chen, J. Zhang, ChemCatChem 2 (2010) 1552–1554.
- [5] S. Liu, X. Wu, W. Liu, W. Chen, R. Ran, M. Li, D. Weng, J. Catal. 337 (2016) 188–198.
- [6] F. Vindigni, M. Manzoli, T. Tabakova, V. Idakiev, F. Bocuzzi, A. Chiorino, Phys. Chem. Chem. Phys. 15 (2013) 13400–13408.
- [7] M. Haneda, T. Kaneko, N. Kamiuchi, M. Ozawa, Catal. Sci. Technol. 5 (2015) 1792–1800.
- [8] M. Liu, S. Wang, T. Chen, C. Yuan, Y. Zhou, S. Wang, J. Huang, J. Power Sour. 274 (2015) 730–735.
- [9] T.F. Hou, S.Y. Zhang, T.K. Xu, W.J. Cai, Chem. Eng. J. 255 (2014) 149–155.
- [10] C.T. Campbell, C.H.F. Peden, Science 309 (2005) 713–714.
- [11] W. Cai, F. Chen, X. Shen, L. Chen, J. Zhang, Appl. Catal. B 101 (2010) 160–168.
- [12] L. Xu, L. Wang, Environ. Sci. Technol. 46 (2012) 10145–10153.
- [13] S.Y. Hao, J. Hou, P. Aprea, F. Pepe, Appl. Catal. B 160 (2014) 566–573.
- [14] T. Divya, N.K. Renuka, J. Mol. Catal. A-Chem. 408 (2015) 41–47.
- [15] F. Chen, X. Shen, Y. Wang, J. Zhang, Appl. Catal. B 121–122 (2012) 223–229.
- [16] J.S. Mu, L. Zhang, G.Y. Zhao, Y. Wang, Phys. Chem. Chem. Phys. 16 (2014) 15709–15716.
- [17] G.M. Mullen, L. Zhang, E.J. Evans, T. Yan, G. Henkelman, C.B. Mullins, J. Am. Chem. Soc. 136 (2014) 6489–6498.
- [18] K. Zhou, X. Wang, X. Sun, Q. Peng, Y. Li, J. Catal. 229 (2005) 206–212.
- [19] C. Sun, H. Li, L. Chen, Energy Environ. Sci. 5 (2012) 8475–8505.
- [20] D. Jiang, W. Wang, L. Zhang, Y. Zheng, Z. Wang, ACS Catal. 5 (2015) 4851–4858.
- [21] E. Aneggi, D. Wiater, C. de Leitenburg, J. Llorca, A. Trovarelli, ACS Catal. 4 (2014) 172–181.
- [22] M.L. Tana, J. Zhang, H.J. Li, Y. Li, W.J. Li, Shen, Catal. Today 148 (2009) 179–183.
- [23] Z. Wu, M. Li, S.H. Overbury, J. Catal. 285 (2012) 61–73.
- [24] T.X.T. Sayle, S.C. Parker, D.C. Sayle, Phys. Chem. Chem. Phys. 7 (2005) 2936–2941.
- [25] M. Nolan, J.E. Fearon, G.W. Watson, Solid State Ionics 177 (2006) 3069–3074.
- [26] Y. Chen, S.H. Lv, C.L. Chen, C.J. Qiu, X.F. Fan, Z.C. Wang, J. Phys. Chem. C 118 (2014) 4437–4443.
- [27] X.P. Wu, X.Q. Gong, Phys. Rev. Lett. 116 (2016) 086102.
- [28] H.X. Mai, L.D. Sun, Y.W. Zhang, R. Si, W. Feng, H.P. Zhang, H.C. Liu, C.H. Yan, J. Phys. Chem. B 109 (2005) 24380–24385.
- [29] E.G. Heckert, S. Seal, W.T. Self, Environ. Sci. Technol. 42 (2008) 5014–5019.
- [30] J.C. Dupin, D. Gonbeau, P. Vinatier, A. Levasseur, Phys. Chem. Chem. Phys. 2 (2000) 1319–1324.
- [31] S. Tsunekawa, T. Fukuda, A. Kasuya, Surf. Sci. 457 (2000) L437–L440.
- [32] Y.H. Wang, F. Wang, Q. Song, Q. Xin, S.T. Xu, J. Xu, J. Am. Chem. Soc. 135 (2013) 15056–1515.
- [33] V.V. Pushkarev, V.I. Kovalchuk, J.L. d'Itri, J. Phys. Chem. B 108 (2004) 5341–5348.
- [34] G.S. Herman, Y.J. Kim, S.A. Chambers, C.H.F. Peden, Langmuir 15 (1999) 3993–3997.
- [35] C. Fang, D.S. Zhang, L.Y. Shi, R.H. Gao, H.R. Li, L.P. Ye, J.P. Zhang, Catal. Sci. Technol. 3 (2013) 803–811.
- [36] M. Aslam, M.T. Qamar, M.T. Soomro, I.M.I. Ismail, N. Salah, T. Almeelbi, M.A. Gondal, A. Hameed, Appl. Catal. B 180 (2016) 391–402.
- [37] D.R. Mullins, P.M. Albrecht, T.L. Chen, F.C. Calaza, M.D. Biegalski, H.M. Christen, S.H. Overbury, J. Phys. Chem. C 116 (2012) 19419–19428.
- [38] M. Molinari, S.C. Parker, D.C. Sayle, M.S. Islam, J. Phys. Chem. C 116 (2012) 7073–7082.
- [39] X. Liang, Z. He, Y. Zhong, W. Tan, H. He, P. Yuan, J. Zhu, J. Zhang, Colloids Surf. A 435 (2013) 28–35.
- [40] Y.J. Wang, H. Dong, G.M. Lyu, H.Y. Zhang, J. Ke, L.Q. Kang, J.L. Teng, L.D. Sun, R. Si, J. Zhang, Y.J. Liu, Y.W. Zhang, Y.H. Huang, C.H. Yan, Nanoscale 7 (2015) 13981–13990.
- [41] M. Nolan, S.C. Parker, G.W. Watson, Phys. Chem. Chem. Phys. 8 (2006) 216–218.
- [42] Y. Wang, X. Shen, F. Chen, J. Mol. Catal. A: Chem. 381 (2014) 38–45.
- [43] L. Ge, T. Chen, Z.Q. Liu, F. Chen, Catal. Today 224 (2014) 209–215.
- [44] W. Huang, Y. Gao, Catal. Sci. Technol. 4 (2014) 3772–3784.
- [45] Z. Wu, M. Li, D.R. Mullins, S.H. Overbury, ACS Catal. 2 (2012) 2224–2234.
- [46] J.C. Conesa, Surf. Sci. 339 (1995) 337–352.
- [47] X. Xie, Y. Li, Z.Q. Liu, M. Haruta, W. Shen, Nature 458 (2009) 746–749.
- [48] D. Jiang, W. Wang, L. Zhang, R. Qiu, S. Sun, Y. Zheng, Appl. Catal. B 165 (2015) 399–407.
- [49] P. Ji, J. Zhang, F. Chen, M. Anpo, Appl. Catal. B 85 (2009) 148–154.